https://dx.doi.org/10.1016/j.rse.2021.112834

Modeling the direction and magnitude of angular effects in nighttime light remote sensing

Xiaoyue Tan [a], Xiaolin Zhu [a,*], Jin Chen [b], Ruilin Chen [b]

[a] Department of Land Surveying and Geo-Informatics, The Hong Kong Polytechnic University, Hong Kong, China

[b] State Key Laboratory of Remote Sensing Science, Faculty of Geographical Science, Beijing Normal University, Beijing 100875, China

*Corresponding author:

Xiaolin Zhu

Address: The Hong Kong Polytechnic University, Room ZS621, South Wing, Block Z, 181 Chatham Road South, Kowloon, Hong Kong.

Phone: +852-2766-5976; Email: xiaolin.zhu@polyu.edu.hk

Abstract

Remote sensing of nighttime light (NTL) offers a unique opportunity to monitor urban dynamics and human socioeconomic activity directly from space. However, angular observations lead to inconsistencies among observations over the same area on different days, introducing uncertainty into daily NTL time series. This study aims to investigate this angular effect and its drivers using the Visible Infrared Imaging Radiometer Suite/Suomi (VIIRS) Black Marble NTL dataset. First, we proposed a conceptual model of the angular effect and hypothesized the mechanism of how urban three-dimensional (3D) landscapes form the anisotropic characteristics of artificial light observations. Second, we quantified the spatial patterns of the angular effect within five representative cities, and identified three distinctive types of angular effects: negative, U-shaped, and positive. Subsequently, the contribution of landscape factors to the direction (i.e., the type) and magnitude (i.e., NTL change rate with angle) of the angular effect is quantified using multinomial logistic regression and mediation analyses, respectively. The results show that the direction of the angular effect is mainly controlled by building height which determines the blocked and visible parts of artificial light at different satellite viewing angles. The magnitude of the angular effect is determined by both NTL brightness and landscape factors. The mediation analysis shows that landscape factors can have a direct effect on the magnitude of the angular effect as well as an indirect effect on the magnitude by affecting NTL brightness. Among the landscape factors, both vegetation and buildings are indicated to be significantly influential factors with direct and indirect effects. The findings of this research deepen our understanding of the NTL angular effect, guide the development of technologies for reconstructing high-quality daily NTL time series by correcting the angular effect, and help us better monitor high-frequency socioeconomic activities.

Keywords: nighttime light, VIIRS DNB, Black Marble, angular effect, artificial light radiance

Introduction

Nighttime light (NTL) remote sensing provides a unique perspective to explore the spatial distribution of human activities effectively (Levin et al., 2020) and has yielded valuable insights in quantifying and tracking urban dynamics and their environmental impacts (Zhao et al., 2019). Currently, several satellites that can detect artificial light at night have been launched and have provided NTL products at different spatial and temporal resolutions. Among them, the most popular NTL products are derived from the Defense Meteorological Satellite Program/Operational Linescan System

(DMSP/OLS) and the Day/Night Band (DNB) of the Visible Infrared Imaging Radiometer Suite/Suomi National Polar-Orbiting Partnership (VIIRS/NPP) satellite. These NTL products, especially the annual and monthly compositions, have been widely used in numerous applications, such as urbanization mapping (Imhoff et al., 1997; Zhou et al., 2018), socioeconomic activity detection (Elvidge et al., 2009; Ge et al., 2018), conflict and disaster detection (Elliott et al., 2015; Li et al., 2017), energy consumption estimation (Elvidge et al., 2016; Shi et al., 2018), and light pollution assessment (Kyba et al., 2017).

While annual and monthly NTL products are the dominant applications, daily NTL data have also played an irreplaceable role in monitoring rapid changes in human activities and environments, such as natural disasters (Zhao et al., 2018), power outages (Cao et al., 2013), lighting power consumption (Román & Stokes, 2015), fire detection (Polivka et al., 2016), fire phase characterization (Wang et al., 2020), and air quality monitoring (Wang et al., 2016). However, the daily light radiance observed by satellites has considerable uncertainty for various reasons (Coesfeld et al., 2018; Levin et al., 2020; Wang et al., 2021), such as atmospheric conditions (Fu et al., 2018), moonlight (Cao et al., 2019; Zeng et al., 2018), seasonal variations in snow cover and vegetation (Levin, 2017), differences in satellite viewing angle (Kyba et al., 2013; Li et al., 2019), and data acquisition time at night (Baráet al., 2019). Recently, Román et al. (2018) proposed a set of algorithms to eliminate the uncertainties in NPP/VIIRS DNB observations and developed the Black Marble suite. The key technologies of this strategy include lunar irradiance modeling; an atmospheric correction to compensate for aerosol impacts on observed NTL radiance; a bidirectional reflectance distribution function (BRDF) correction to remove biases introduced by moonlight, aerosol, and surface albedo; and a seasonal correction to mitigate errors stemming from seasonal vegetation canopy change. On this basis, a state-of-the-art NTL product, the Daily Lunar BRDF Adjusted Nighttime Lights dataset (VNP46A2), was published by the National Aeronautics and Space Administration (NASA) in 2020.

Despite the advanced NTL radiance correction strategy, angular effects still exist in the daily NTL time series, especially for artificial light. This is because angular effects, also known as anisotropic features of artificial light observations, are still not considered in the Black Marble suite (Román et al., 2018; Wang et al., 2021). Since DMSP/OLS and NPP/VIIRS are wide-view sensors with a maximum viewing zenith angle (VZA) of over 60° and swath widths greater than 3000 km, the accumulated radiance variation can be rather large even when other observation conditions remain constant (Levin et al., 2020). Several studies have been conducted to explore the characteristics and have proposed some possible driving factors of angular effects. Johnson et al. (2013) found that the VIIRS DNB radiance over a city decreases by approximately 30% as the VZA goes from 60° to nadir. Bai et al. (2015) observed that the light intensity of some isolated sites (e.g., bridge lights, oil platforms) reached its lowest value at nadir and increased toward the edge of the scan. The causes of these results may include atmospheric path length at different viewing angles, point spread function differences along with the scan, atmospheric scattering, and airglow. Some researchers suggest that NTL radiance in urban areas may have different angular emission profiles with regard to the local landscape, such as tall buildings, trees, and vertical light sources (Coesfeld et al., 2018; Kyba et al., 2015; Levin et al., 2020; Tong et al., 2020). Recent research has further confirmed this inference by analyzing the NTL-VZA relationship at selected points in several cities around the globe and has found that NTL radiance increases with the VZA over residential areas (Li et al., 2019), while the NTL radiance decreases with increasing VZA in commercial areas with tall buildings (Wang et al., 2021). Additionally, the NTL radiance decreases and then increases with the VZA (i.e., U-shape) at some sites, forming a hot spot effect similar to the daytime BRDF.

The angular effect may stem errors in time-series analysis, but on the other hand, it provides additional information about urban structures (Levin et al., 2020). Therefore, while recognizing the necessity of quantifying and understanding the angular effect, further investigation is needed. First, current studies have been conducted on limited sites, making it unclear whether the angular effect exists at different sites throughout a city with various urban landscapes and functions and what spatial pattern the effect has. Second, current studies have only focused on the shape of the angular effect and ignored its intensity. Thus, a comprehensive quantitative model that considers the type and magnitude of the angular effect is needed to explore its mechanisms. Third, the current qualitative analysis has determined that building height is a significant factor shaping the angular effect, but the influences of buildings, roads and other landscape factors have not been explored in detail. Last, existing nighttime shortwave radiative transfer models (RTM) are lacking 3D geometry, which is one of the most significant sources of uncertainty in the RTMs (Wang et al., 2020; Wang et al., 2021). A deeper understanding of the angular effect and its associations with the urban 3D landscape will give insight into the future development of RTMs.

On this basis, to address the above research gaps, this research aims to quantify the angular effect and understand its driving factors by (1) constructing a conceptual model to describe how the urban landscape forms the NTL angular effect, (2) characterizing the spatial pattern of the NTL angular effect in selected cities, and (3) quantifying the impact of landscape factors on the NTL angular effect using sophisticated statistical models and fine-resolution 3D urban data. The findings of this research will deepen our understanding of the NTL angular effect, guide the development of technologies for reconstructing high-quality daily NTL time series by correcting the angular effect, and finally help us better monitor high-frequency socioeconomic activities.

2 Study material

2.1 Study area

To examine the impact of the urban landscape on the angular effect, we selected five representative cities in North America that hold diverse urban landscape structures: Toronto, New York, Los Angeles, Austin, and Boston. In addition, all the selected cities have reliable electric power systems and do not suffer from disasters or conflicts that may have caused blackouts during the investigated period. These highly developed urban areas generally do not experience intensive land cover changes which can avoid large-scale changes in artificial light sources. Another important reason for selecting these five cities is because 3D models of these cities are available. Three-dimensional city models are necessary datasets for deriving the landscape factors considered in this study.

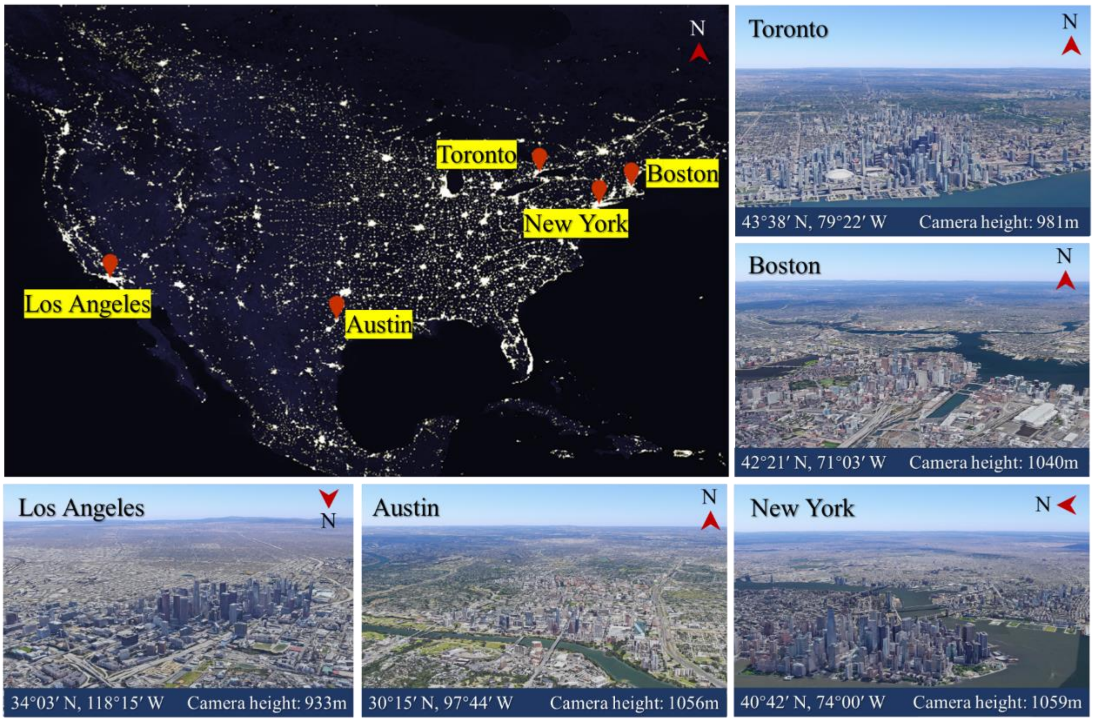

Fig. 1. Location and Google Earth 3D images of the five selected cities. Background NTL image from NASA (https://earthobservatory.nasa.gov/features/NightLights).

2.2 Data

All Black Marble daily level-3 products (https://blackmarble.gsfc.nasa.gov) NTL images taken in 2014 were used in this study to investigate the angular effect. Currently, two Black Marble daily products are publicly available at a 15-arc-second resolution, namely, the daily at-sensor top of atmosphere nighttime radiance product (VNP46A1) and the daily moonlight-adjusted NTL product (VNP46A2). Lunar

BRDF-corrected NTL and the corresponding quality layer from VNP46A2 were used to reduce disturbances from cloud contamination, atmospheric conditions, moonlight, stray light, and seasonal variances in vegetation. Considering the uncertainties existing in the NTL retrieval process (Wang et al., 2021), an orbit-based composition method was proposed in the methodology section to mitigate the uncertainties. The satellite zenith angle was collected from the zenith angle layer provided in VNP46A1. The satellite viewing angles include both the zenith angle and azimuth angle. In this study, we only considered the zenith angle to investigate the NTL angular effect because (1) the daily NTL observations are concentrated in two major azimuth angles, one east and another west (not due east and due west, see Fig. S1. (a) in the Supplementary Data); (2) these two major azimuth angles have no significant impact on the angular effect modeling in our study area (Fig. S1. (b) in the Supplementary Data); and (3) current studies have demonstrated that the zenith angle alone can model the angular effect well, while adding the azimuth angle does not significantly improve the model (Li et al., 2019; Wang et al., 2021).

To characterize the local landscape, we used building information from 3D city models, road information from OpenStreetMap (OSM), and vegetation information from Moderate Resolution Imaging Spectroradiometer (MODIS) products. Three-dimensional city models of selected cities were collected from government open data platforms or local planning and development agencies, providing building footprints with accurate heights in shapefile format. OSM is an open-access worldwide crowdsourcing map that offers elaborate road features of our selected cities. The normalized difference vegetation index (NDVI) from MOD13Q1 (MODIS/Terra Vegetation Indices 16-Day L3 Global 250 m) was selected to calculate the proxy indicating local vegetation cover. Land cover data for the selected cities were derived from the 30-meter Global Land Cover Datasets (Globeland30) Version 2020, and ten land cover classes, including artificial surfaces, cultivated lands, forests, grasslands, shrublands, wetlands, and water bodies, were identified in the product. Land cover data were subsequently used to restrict the areas in which the analysis was conducted. The boundaries of selected cities were downloaded from the city's government open data platforms.

3. Methodology

3.1 Conceptual model of the angular effect

Generally, light sources in cities are located on the ground (e.g., street lamps, car lights, decorative lighting) and vertical surfaces (e.g., signs, curtain walls, light escaping windows). Various factors may affect the light intensity received by a sensor at different view angles, thus causing the angular effect. As reviewed in the introduction section, these factors are broadly related to the ground morphology and the light transmission path. For the Black Marble lunar BRDF-adjusted NTL product that is used in this research, the impacts of factors in the light transmission path (e.g., atmospheric path length, atmospheric scattering) were alleviated after the atmospheric and lunar BRDF correction procedures. However, bias induced by urban morphology varies from place to place and is difficult to correct using general methods. Therefore, the angular effect from artificial light is mainly determined by the local landscape, i.e., ground morphology.

The angular effects can be characterized in two aspects: direction and magnitude. Direction is the general trend, e.g., negative, positive, or other nonlinear forms, of the satellite-observed NTL radiance against the VZA, while the magnitude indicates the NTL change rate with the VZA, i.e., how much radiance changes per degree of angle. Therefore, to understand the formation of angular effects, we proposed a conceptual model to explain how urban landscapes shaped the direction and magnitude of the angular effect. As shown in Fig. 2, we assumed that the local landscape integrated with the viewing angle jointly determines the visible and blocked portions of artificial light radiance, which, together with the surface reflectance, ultimately created an angular effect with a specific direction and magnitude. The landscape may affect the following aspects. (1) Blocking effect: Lights from the ground and vertical surfaces tend to be blocked by nearby buildings, trees, and other objects when satellites observe from large zenith angles, especially in areas with dense high-rise buildings. Depending on the height of light sources and the local geometry, the blocking effect generally increases with the VZA. (2) Visibility changes: Lights from vertical surfaces are barely visible at nadir. As the VZA increases, the satellite receives more light from vertical surfaces, and thus, the observed NTL radiance will rise if the blocking effect remains unchanged. (3) Surface reflectance and BRDF: diverse landscapes and corresponding materials have different reflectance and anisotropic reflection properties that determine how much artificial light can be reflected upwards. However, considering that the reflected light may come from all directions and that the anisotropic reflections of different materials can cancel each other out, the effects of surface reflectance and BRDF properties are neglected in the angular conceptual model.

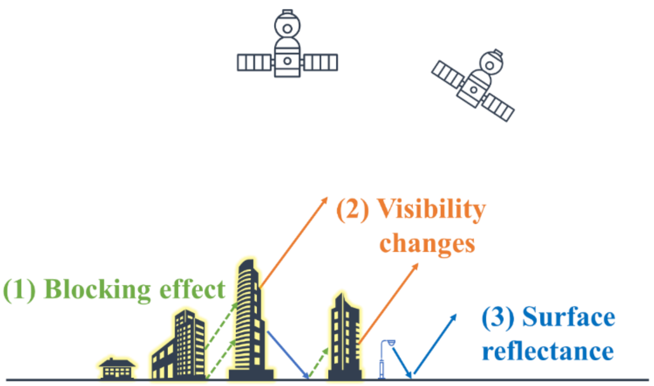

Fig. 2. Sketch of the conceptual model depicting three typical sources of the angular effect: (1) blocking effect, (2) visibility changes, and (3) surface reflectance and BRDF.

Accordingly, as the VZA changes, both the blocking effect and visibility change may cause angular effects in different directions. If the blocked light is much stronger than the increase in visibility, the satellite-observed NTL radiance decreases as the VZA increases, creating a negative angular effect. Conversely, if the visibility increases more than the blocking effect, the satellite-observed light values increase with the VZA, forming a positive angular effect. If the dominance of the blocking effect and visibility reverses with increasing viewing angle, a U-shaped angular effect trend may be present. Some samples in Los Angeles were used to illustrate the above three hypothesized scenarios (Fig. 3 (a)). Specifically, for Site A in the Los Angeles CBD, the scatter plot between the NTL radiance and the VZA shows a negative angular effect (Fig. 3 (b)). This is because lights from the ground can only be observed near the nadir, and a considerable number of floodlit facades and illuminated signs are blocked by nearby high-rising buildings when viewing obliquely. Site B is located in a residential area with low-rise houses that hardly block the ground lights, resulting in a positive angular effect (Fig. 3 (c)). Site C is located in an industrial area that holds large buildings of medium height, causing a competitive relationship between the blocked and visible lights and thus inducing a U-shaped angular effect (Fig. 3 (d)).

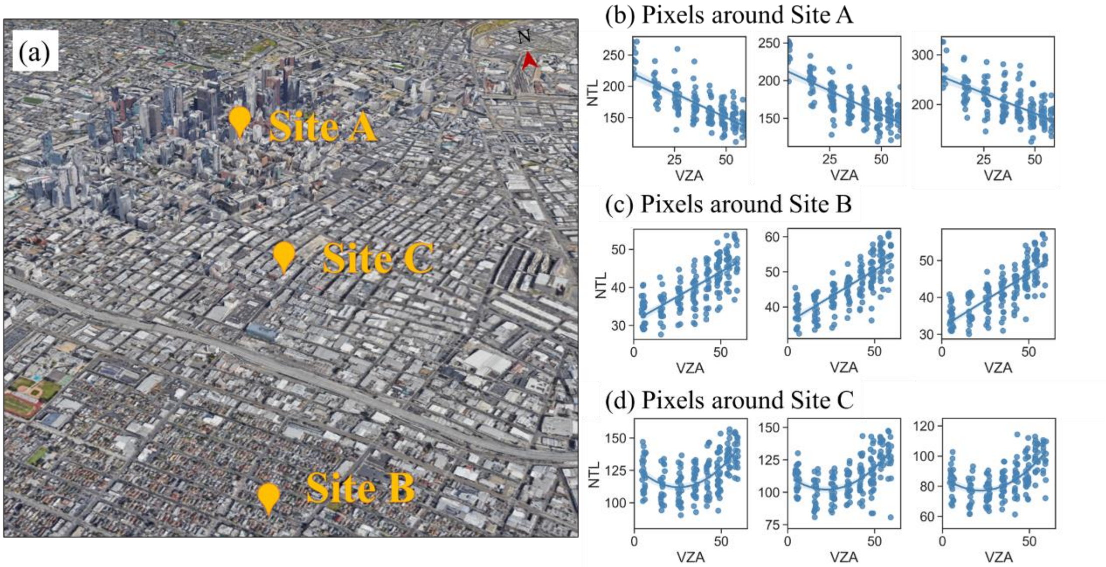

Fig. 3. Samples of angular effect and landscape. (a) Google Earth 3D image around the Los Angeles CBD; (b) VZA-NTL scatters of the negative angular effect samples at site A; (c) VZA-NTL scatters of the positive angular effect samples at site B; (d) VZA-NTL scatter diagrams of the U-shape angular effect samples at site C.

The magnitude of the angular effect, i.e., the rate of the NTL radiance change with the VZA, is another vital feature of the angular effect. As the combined result of multiple landscape factors, the magnitude of angular effects varies between and within cities. To further investigate the impact of the landscape on the magnitude of the angular effect, we quantified the NTL radiance observed at zenith angle θ as L_{θ}:

$$L_\theta = aL_s \cdot f_1(\theta) + (1-a)L_s \cdot f_2(\theta) \quad (1)$$

where a is the portion of upwards emissions of surface light sources, and (1- a) is the portion of downwards emissions, L_s is the actual surface light emission, and $f_1(\theta)$ and $f_2(\theta)$ are the impacts of the viewing angle. According to the conceptual model, the following equations can be obtained:

$$f_1(\theta) = V(\theta) \cdot B(\theta) \quad (2)$$

$$f_2(\theta) = R(\theta) \cdot V(\theta) \cdot B(\theta) \quad (3)$$

where $V(\theta)$ and $B(\theta)$ represent the visibility and blocking effect at VZA θ, respectively. $R(\theta)$ is the hemispheric-directional reflectance at the VZA θ considering that downwards lights in VIIRS/DNB pixels may come from different sources (e.g., windows, streetlights, billboards) and all directions. For the negative and positive angular effects, we define the magnitude as the slope of the NTL radiance change from nadir to the largest VZA as in Eq. (4):

$$Magnitude = \left|\frac{\Delta L_\theta}{\Delta\theta}\right| = \left|\frac{aL_s \cdot V(\Delta\theta) \cdot B(\Delta\theta) + (1-a)Ls \cdot R(\Delta\theta) \cdot V(\Delta\theta) \cdot B(\Delta\theta)}{\Delta\theta}\right| \quad (4)$$

Since the range of viewing angle θ at different locations is basically the same from nadir to nearly 70° for the NPP satellite and the variability in the visibility $V(\Delta\theta)$, blocking effect $B(\Delta\theta)$ and reflectance factor $R(\Delta\theta)$ are all dependent on the landscape characteristics and geometry, we subsequently infer that the magnitude of the angular effect is a function of L_s and *landscape*.

$$Magnitude = f(L_s, Landscape) \quad (5)$$

Since the actual surface light emission L_s is unavailable due to the large daily variation caused by aerosols and other surface changes (e.g., snows, vegetation), we used the average value of orbit-composed VZA-NTL pairs to approximate the actual artificial lights considering that the five cities did not experience large disturbance in the year of 2014. As shown in Fig. 4, the orbit-based composition can greatly reduce the variations from daily data, thus their average value can represent the average situation of light emissions of a pixel.

For landscape factors, several indicators regarding roads, buildings, and trees were derived from geo-information data and remote sensing products to represent the local landscape in this research. Road length is a reasonable indicator, as streetlights and car lights are significant artificial light sources at night. The road length in each grid cell was calculated using OSM data. We used the attribute labels to filter out roads that may not have been equipped with lighting facilities, such as footways, paths, steps, pedestrians, and tracks. The average building height, the average footprint area, and the number of buildings in each grid cell were calculated to represent the local geometric characteristics. NDVI was used as a proxy for vegetation-blocked lights and the altered BRDF characteristics of artificial surfaces. The 95th percentile NDVI values were derived from a one-year time series and then resampled to the resolution of the NTL radiance data to quantify the amount of vegetation in each grid cell.

3.2 Angular effect quantification and classification

To test the proposed conceptual model and confirm the hypothesized types of angular effects, the spatial patterns of the angular effects of the five cities were precisely characterized at the spatial resolution of the VNP46A2 product (i.e., 15 arc-seconds). First, we kept only the high-quality and confidently clear pixels according to the quality layer and cloud mask layer. To avoid NTL observations that may have been affected by snow (Wang et al., 2021), we discarded images collected between December and March in Toronto, Boston, and New York according to the 2014 weather records. Second, considering the geographic mismatch induced by the differences in the DNB view geometry over days, we applied a 3×3-pixel moving average to extract an NTL time series for each grid, as recommended by recent research (Román et al., 2018; Wang et al., 2021). Finally, we appended two filtering procedures to remove undetected poor-quality data after visually examining the processed NTL data. The first filtering discarded data that fell outside the two standard deviations for each NTL time series. The second filtering discarded images acquired on cloudy nights. The accuracy of the nighttime cloud mask provided in the

Black Marble dataset is relatively lower (global hit rate of 86.4%) than daytime, both leakage and false alarm exist in the nighttime cloud mask (Wang et al., 2021). We found that many clouded pixels were not masked when the whole city was mostly cloudy. Thus, we set an empirical threshold: when over 60% of pixels in a city were identified as cloudy by the quality layer, the whole image was discarded.

Quantifying the relationship between the viewing angle and satellite-observed NTL radiance is the key to understanding the angular effect. However, according to our data exploration and previous research (Bai et al., 2015; Li et al., 2019; Wang et al., 2021), it is a common situation that the DNB observations show significant variation in the same viewing angle and location (see blue points in Fig. 3, Fig. 4 and Fig. 7) due to multiple factors. For the Black Marble lunar BRDF-corrected NTL dataset, atmospheric effects dominate retrieval uncertainty since daytime aerosol parameters used in the atmospheric correction process are often different from nighttime (Wang et al., 2021; Zhou et al., 2021). Other factors mainly involve upstream data inputs (e.g., coarser nighttime snow cover flag, errors in nighttime cloud mask, misused surface albedo). Noise from other sources may also remain, such as the noise induced by differences in satellite passing time, temporary light sources, time of lights turning on or off, and sensor errors (Coesfeld et al., 2018). To address these issues, we developed a composition method leveraged on the repeatability of satellite orbits to minimize the influence of daily variance in NTL. The SNPP satellite with VIIRS onboard has a sun-synchronous polar orbit and a repeat cycle of 16 days; thus, NTL brightness acquired every 16 days is regarded as a repeated observation on the ground lights at the same viewing angle. Since the median value could exclude the observations with extremely high aerosol loadings or extremely low aerosol loadings, it can represent the average situation of NTL observation at a certain angle. As shown in Fig. 4, by taking the median (orange dots) from each group of repeated observations (blue dots), a maximum of 16 VZA-NTL pairs can be extracted from the whole time series for each grid as the representative observation for each viewing zenith angle. Besides, by selecting the median value among the multiple observations at the same VZA during the year, the generated VZA-NTL data pairs that are subsequently used for modeling angular effect is non-chronological. Thus, the time effect of daily NTL images that may affect modeling results has been largely removed by the orbit composition approach.

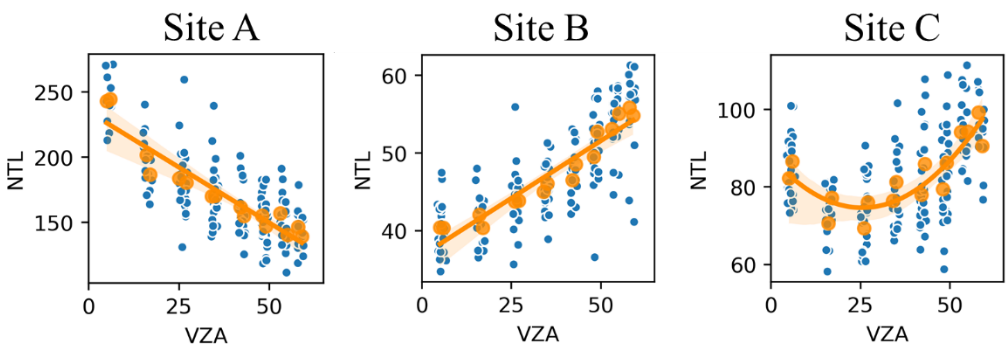

Fig. 4. Examples of extracting stable VZA-NTL pairs using the orbit-based composition method. The blue dots are NTL radiance observations, orange dots are the stable VZA-NTL pairs extracted, and orange curves show the direction of the angular effect. Location of site A, B, and C show in Fig. 3 (a).

The most striking and distinctive feature of the angular effect is direction, i.e., the trend of the VZA-NTL curve. Based on the proposed conceptual model and sample exploration, we assume three typical angular effects in cities: positive, negative and U-shaped. A classification process was developed to capture the predominant direction of the angular effect for each grid cell. In the classification process, two statistical methods, i.e., linear regression (LR, Eq. (6)) and quadratic regression (QR, Eq. (7)), were employed to fit the VZA-NTL pairs:

$$L = \beta_1 \theta + \beta_0 \tag{6}$$

$$L = \beta_2 \theta^2 + \beta_1 \theta + \beta_0 \tag{7}$$

where L is the NTL radiance, θ is the VZA of the observations, β_2 and β_1 are the coefficients of θ^2 and θ, β_0 is the constant in both Eqs. (6) and (7). Then, the direction of the angular effect is identified by comparing the significance at the 0.05 level and the goodness of fit of the two models. Naturally, the R^2 of quadratic regressions is often higher than that of linear regressions involving one more independent variable that leads to overfitting. Thus, we set an empirical threshold of 0.2 to separate the linear increasing/decreasing VZA-NTL trends from the typical U-shaped curves. The classification progress is shown in Fig. 5, where R^2_{LR} and R^2_{QR} are the *R*-squares of linear regression and quadratic regression, respectively, and β_1 is the coefficient in Eq. (6). Nonsignificant means neither linear nor quadratic models are sufficient to depict the angular effect.

Before applying the classification progress, we filtered out grid cells with an annual average radiance of less than 10 nW/cm^2/sr to keep our exploration concentrated in urban areas. The threshold is selected because: (1) more than 80% of pixels in our study area are dominated by the artificial surface when the annual NTL is brighter than 10 nW/cm^2/sr using 30-meter Global Land Cover Datasets (Globeland30) as the reference (see Fig. S2 in the Supplementary Data); and (2) NTL radiance in rural areas can be up to 10 nW/cm^2/sr due to moonlights (Wang et al., 2021). Furthermore, to guarantee the validity of the two regression models, only grid cells with sufficient observations entered the classification progress: more than 20 valid observations in a one-year time series and 10 VZA-NTL pairs.

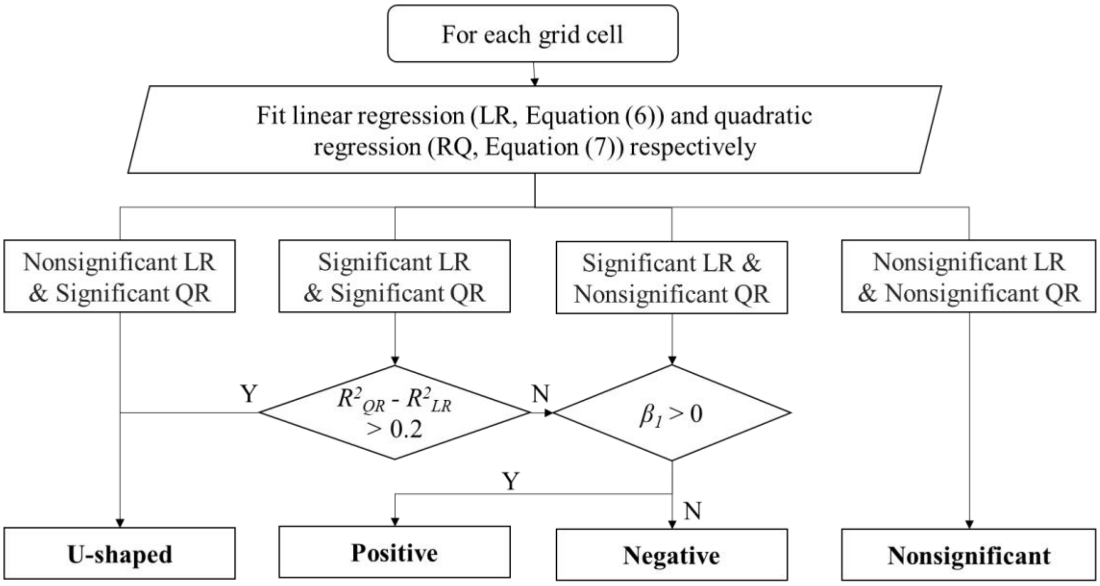

Fig. 5. Classification workflow to identify the direction of the angular effect for each grid cell.

3.3 Statistical method for analyzing the direction of the angular effect

To investigate the impact of landscape on the direction of the angular effect, we applied multinomial logistic regression to grid cells of positive, negative, and U-shaped angular effects for five selected cities. Multinomial logistic regression is an extension of binary logistic regression and is usually used when dependent variables have two or more categories. To assess the impact of independent variables, one category of the dependent variable is chosen as the base category, and the log odds of category m in the dependent variable (y) compared to the base category (b) is calculated as follows:

$$\ln \Omega_{m|b} = \ln \frac{\Pr(y=m|X)}{\Pr(y=b|X)} = X\beta_{m|b} \quad (8)$$

where X represents the explanatory variable and city dummy variables, and $\beta_{m|b}$ is the regression coefficient vector. To control unobserved short-term changes and differences between cities, the city-fixed effect is taken into account in this model by including city dummy variables. Like binary logistic regression, multinomial logistic regression uses maximum likelihood estimation to evaluate the probability of each category.

The relative risk ratio (RRR) is used to interpret the multinomial logistic regression considering that the coefficient predicts the logit of outcome *m* relative to the base group *b*. RRR is the exponentiated value of the multinomial logit coefficients, i.e., $e^{\beta_{m|b}}$ and indicates how the ratio of probability between category *m* and referent category *b* changes for one unit change in the specified independent variable. For example, an RRR = 1 indicates that the probability of the prediction result falling in category *m* equals the probability of the prediction result falling in referent category *b*. An RRR>1 suggests that the probability of category *m* relative to referent category *b* increases with the independent variable, given that other variables in the model remain unchanged. Conversely, an RRR<1 suggests that the probability decreases as the independent variable increases. In this research, we normalized the independent variables before running the multinomial logistic regression to make the RRR of different variables comparable in terms of impact. To evaluate the goodness-of-fit of multinomial logistic regression, McFadden's R-square is applied:

$$R^2_{McF} = 1 - \frac{\ln L_M}{\ln L_0} \tag{9}$$

where L_M is the likelihood function for the estimated model and L_0 is the likelihood function for the intercept model (i.e., no predictors in the model). Thus, a small R^2_{McF} indicates sufficient goodness of fit.

To capture the characteristics of typical angular effect directions and the corresponding influential landscape factors, we set several filtering conditions for the grid cells entering the multinomial logistic regression. First, to consider only artificial surfaces, Globeland30 was used to identify the most widely distributed land cover in each grid cell. Second, grid cells were avoided near the decision boundary of classification. From the classification procedure in Section 3.2, a scenario in which a grid cell has an ambiguous angular effect feature is possible. Therefore, we used the fitness of linear and quadratic regression to filter out grid cells with ambiguous characteristics. For positive and strong angular effects, grid cells with the top 75% R^2_{LR} entered the multinomial logistic regression, and for U-shaped angular effects, grid cells with the top 75% R^2_{QR} entered the multinomial logistic regression.

3.4 Statistical method for analyzing the magnitude of the angular effect

Mediation analysis was applied to investigate how the landscape affects the magnitude of positive, negative, and U-shaped angular effects. As analyzed in the conceptual model, the magnitude is a function of artificial light emission and landscape. Light emissions are also influenced by landscape factors such as buildings and roads. Thus, the causal chain in which landscape affects the angular effect through third variable light emissions is likely to hold. The fact that an independent variable leads to the predictor variable through a third variable is the mediational effect, and the third variable is referred to as the mediator (Baron & Kenny, 1986). In this research, we considered the magnitude of the angular effect as the dependent variable, landscape factors as the independent variables, and the surface light emission L_s as the mediator. According to the mediation analysis approach (MacKinnon et al., 1995), the overall relationship we observed between landscape factors and the magnitude of angular effect (marked as the total effect in Fig. 6 (a)) consists of two pathways (Fig. 6 (b)): (1) the indirect effect, in which landscape factors lead to the magnitude of angular effect through L_s; and (2) the direct effect, in which landscape factors lead to the magnitude of angular effect directly, regardless of the mediator.

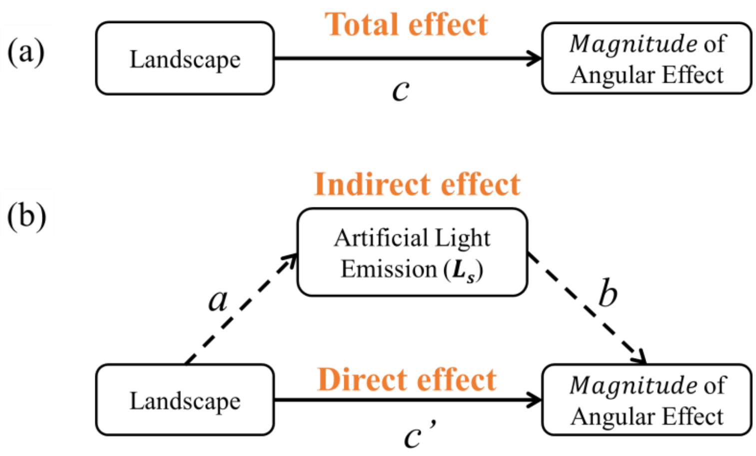

Fig. 6. Sketch of mediation analysis: (a) The overall relationship between independent and dependent variables; (b) The direct and indirect effects between independent and dependent variables.

By estimating the indirect and direct effects and testing their significance, we revealed the path and intensity of the landscape's impact on the angular effect. The classical statistical mediation testing method proposed by Baron and Kenny (1986) has been widely used and proven to be a practical approach to test mediating effects. In this research, we adopted the approach and established the following three regression equations to examine mediation:

$$Magnitude = \beta_0 + c\ Landscape + \mu\ City + \varepsilon \tag{10}$$

$$L_s = \beta_0 + a\ Landscape + \mu\ City + \varepsilon \tag{11}$$

$$Magnitude = \beta_0 + b\ L_s + c^{'} Landscape + \mu\ City + \varepsilon \tag{12}$$

For the positive and negative angular effects, L_s is the actual surface light emission, which can be estimated by the average value of the orbit-composition NTL series; *Magnitude* is the rate of NTL brightness change as described in the conceptual model; *Landscape* represents the independent variables listed in Section 3.1, mainly involving buildings, roads, and vegetation; β_0 and ε are the intercepts and error terms of the equations, respectively; *City* is the city dummy variables to account the unobserved city-fixed effect; and *a, b, c,* and *c'* are the coefficient vectors of each regression equation, also marked with the same letter in Figs. 6 (a) and (b). For the U-shaped angular effect, the landscape's impact on the angular effect was examined from the drop and the rising segments of the U-shape respectively. Previous works (Li et al., 2019; Wang et al., 2021) and our study suggested that quadratic regression model (Eq. (7)) can be used to fit the pattern of the U-shaped angular effect, i.e., the observed NTL radiance first drops and then rises as the satellite zenith angle increases. Thus, the U-shaped angular effect was divided into the drop and the rising segments according to the symmetry axis of the quadratic curve. Here the *Magnitude* of each segment was measured as the radiance difference between the highest and lowest points of the quadratic curve in each segment.

Then, classical four-step testing for mediation was adopted based on Eqs. (10) - (12). The first three steps were to establish zero-order relationships between (1) the independent variables (*Landscape* factors) and the dependent variable (*Magnitude* of angular effect), (2) the independent variables (*Landscape* factors) and mediator (light emission L_s), and (3) the dependent variable (*Magnitude* of angular effect) and mediator (light emission L_s). If the relationships obtained from step 1 to step 3 were all statistically significant, we concluded that the indirect effect was verified. In step 4, we established the relationship using Eq. (12), and if the effect of the independent variable on the *Magnitude* of the angular effect (i.e., the coefficient *c'*) were still significant after controlling for the mediator, partial mediation was supported, i.e., indirect and direct effects existed at the same time (Fig. 6 (b)). If not, full mediation was supported. In addition, the suppression effect was supported if the total effect was nonsignificant due to the opposition of direct and indirect effects with similar values.

The indirect and direct effects indicate the significance of the two pathways shown in Fig. 6 (b). To reveal their contributions to the angular effect, accurate quantification and examination of the indirect and direct effects are essential. The indirect effect was calculated as the product of two regression coefficients (a $\times$ b). This research adopted bootstrapping methods over the conventional Sobel z-test (Baron & Kenny, 1986) (Eq. (13)) to assess the statistical significance of the indirect effect, as has been widely recommended (Hayes, 2017; Preacher & Hayes, 2008; Zhao et al., 2010):

$$z = \frac{a \times b}{\sqrt{b^2 s_a^2 - a^2 s_a^2}} \quad (13)$$

where a and b are unstandardized coefficients in Eqs. (11) and (12) and s_a and s_b are the standard errors of a and b, respectively. The total effect of the independent variable on dependent variable c can be expressed as the sum of indirect and direct effects:

$$c = c' + ab \quad (14)$$

where *c* and *c'* are unstandardized regression coefficients in Eqs. (10) and (12).

4 Results and analysis

4.1 Spatial pattern of angular effect

Fig. 7 shows the radiance and VZA of typical grid cells with three identified directions of the angular effect in the selected cities. The VZA-NTL relationship of all samples is significant with p-value less than 0.05. The scatter diagrams show that significant variance existed in NTL radiance observations even at the same view angle (blue dots), while the VZA-NTL pairs (orange dots) produced by the orbit-based composition method could capture the direction of angular effect.

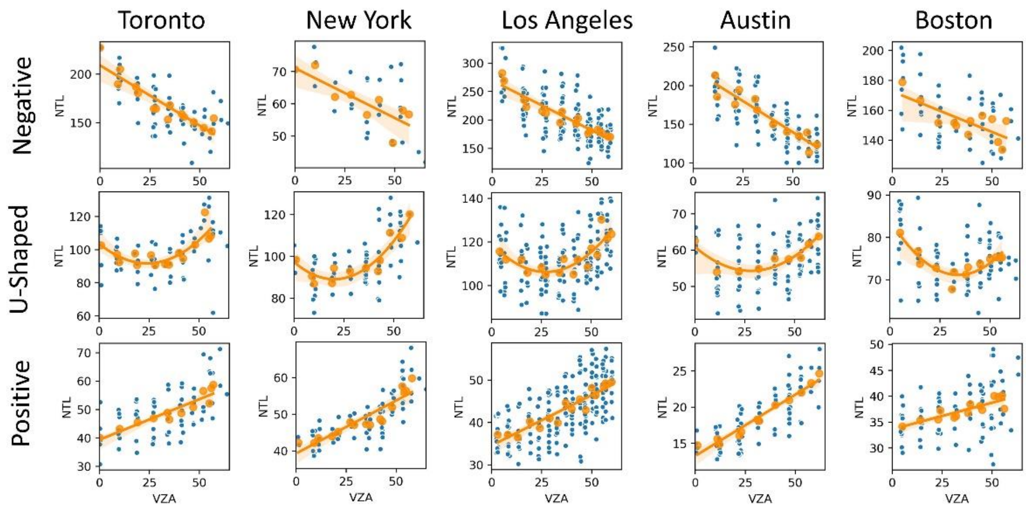

Fig. 7. Scatter plots of VZA and NTL radiance for typical samples. The blue dots are NTL observations, and orange curves show the direction of the angular effect detected from stable VZA-NTL pairs (orange dots).

The NTL brightness, angular effect directions, and building height across the selected 5 cities are plotted in Figs. 8 (a) - (c). The negative angular effect exists in brighter core built-up areas where the central business district (CBD) is usually located (red areas in Fig. 8 (c)), while positive and U-shaped angular effects are widely present in other areas in each city. Furthermore, the distribution of the angular effect direction seems to show a concentric circle structure, negative grid cells in the central area, U-shaped and positive grid cells to the outside. To determine this spatial pattern, we calculated the annual average NTL radiance and angular effect coefficient (i.e., Pearson correlation coefficient between VZA and NTL) in each 1-km-buffer ring from the brightest grid cell in the urban center outwards (example buffer zones of every 5 km shown in Fig. 8 (a)). As illustrated in Fig. 8 (d), the negative angular effect coefficient was predominant in the first few buffer rings, which were also the brightest areas, indicating that satellite-observed NTL radiance decreases with the VZA in an urban center. As it proceeded outwards, the NTL brightness sharply decreased, while the average angular effect coefficient increased dramatically to a positive value.

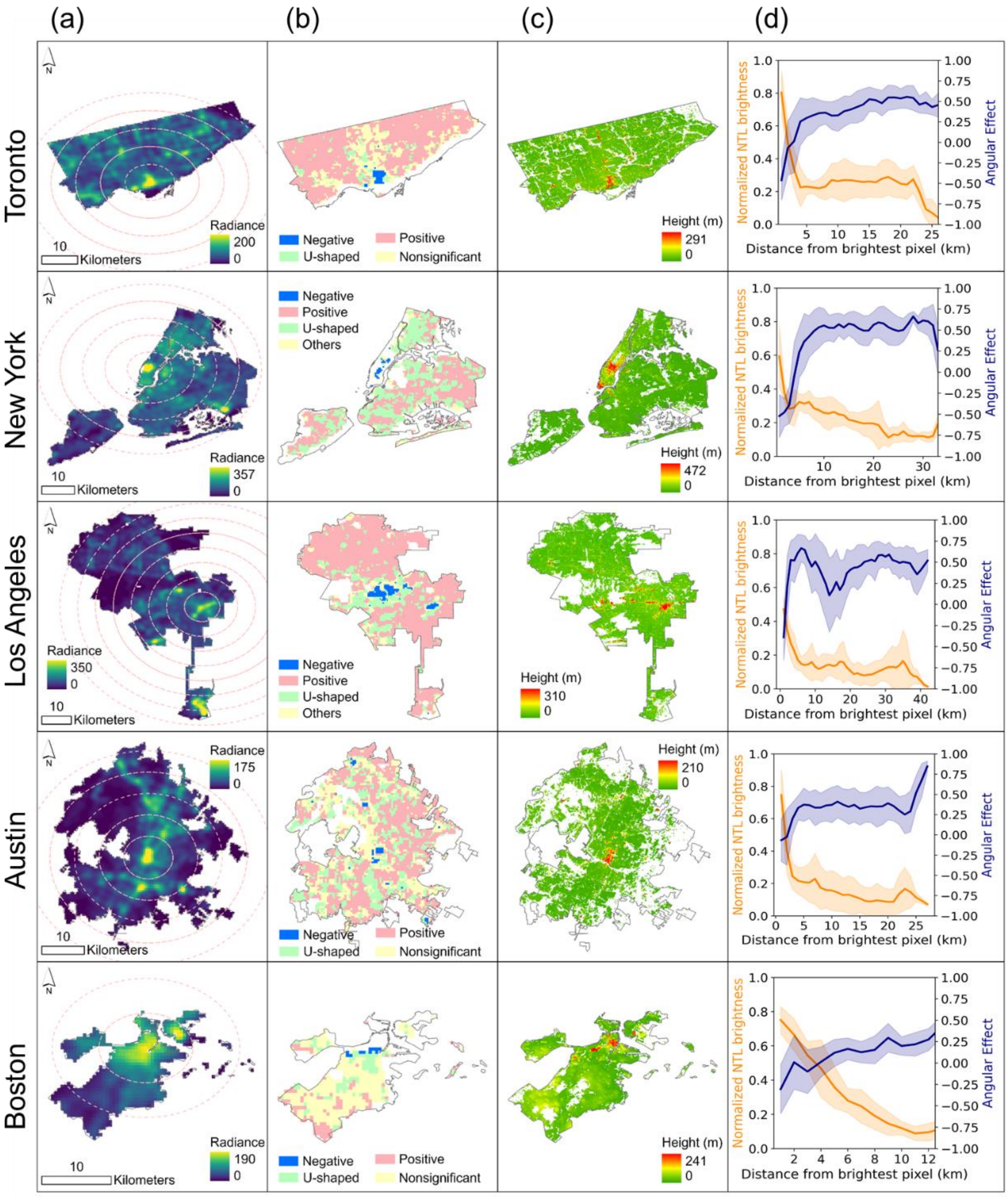

Fig. 8. (a) Spatial distribution of annual average NTL brightness, the pink dashed circle shows the buffer zones at an interval of 5 km and the brightest region as the center; (b) Spatial distribution of different angular effect directions; (c) Building height maps; (d) Changes in average NTL radiance (orange curve) and angular effect coefficient (purple curve) outwards from the urban center. The shadow represents the

standard deviation.

4.2 Direction of angular effect

Table 1 shows the multinomial logistic regression results of negative and positive angular effects, both estimated relative to the U-shaped angular effect. Since the independent variables were standardized before estimating the logistic model, the relative risk ratio (RRR) indicates a multiplicity of change in the likelihood of negative/positive with an increase of one standard deviation (rather than one unit) in the landscape factor while keeping other independent variables unchanged. McFadden's R-square of the estimated model is 0.18, suggesting a much better fitness than that of the intercept model.

Table 1. Multinomial logistic regression results for negative and positive angular effects with U-shaped angular effect as the base category, coefficients of city fixed-effect dummy variables not presented.

	Negative		Positive	
	Relative Risk Ratio	Std. Err.	Relative Risk Ratio	Std. Err.
Road Length	1.325**	0.089	0.948	0.028
NDVI	1.077	0.166	0.968	0.035
Building height	1.547**	0.128	0.559**	0.04
Building size	0.630*	0.135	0.986	0.037
Building number	0.510**	0.089	1.364**	0.05
Constant	0.027**	0.009	2.484**	0.185
City-fixed effects	Yes	Yes	Yes	Yes

Robust seeform in parentheses
** p<0.01, * p<0.05

For the estimated results of the negative angular effect, the increase in building height and road length made a positive contribution, while the size and number of buildings were negatively correlated with the negative angular effect. NDVI was not statistically significant in the negative angular effect model at a 95% confidence level, indicating that an increase in NDVI does not cause a significant change in the likelihood of the outcome category. For the positive angular effect, building height contributes negatively to the risk ratio of the positive angular effect relative to the U-shaped angular effect while the number of buildings contributes positively.

We found that different directions of the angular effect were associated with certain landscape features from the estimated models. The difference in estimated RRR in building height indicated that it is one of the most significant driving factors for the three distinct directions of the angular effect. The negative angular effect was present in high-rise building areas, such as the CBD, where the average height exceeded those of other districts. The positive angular effect was accompanied by low buildings, and a U-shaped angular effect was present in areas with medium-height buildings. Specifically, for one standard deviation increase in building height (6.765 m) in a grid cell, the possibility of a negative angular effect is expected to increase by a factor of 1.547, whereas the possibility of a positive angular effect decreases by a factor of 0.559. This finding statistically confirms the characterization of building height as a vital decisive factor in the angular effect as found in previous research (Li et al., 2019; Wang et al., 2021).

The amount and size of buildings in a grid cell are also important landscape features contributing to a particular angular effect. As shown in Table 1, the increase in the number of buildings will significantly decrease the possibility of a negative angular effect and increase the possibility of a positive angular effect. The regression results in Table 1 also indicate that grid cells with positive and U-shaped angular effects are similar in size (nonsignificant RRR), while increases in building size will considerably reduce the likelihood of a negative angular effect. This is corroborated by the spatial distribution analysis in Section 4.1. Both positive and U-shaped angular effect grid cells are predominated by residential areas or industrial districts, leading to larger numbers and average footprint areas than areas with negative angular effects. By contrast, areas with negative angular effects are usually dominated by higher buildings with larger distances than residential areas.

4.3 Magnitude of the angular effect

The contribution of driving factors to the magnitude of the positive and negative angular effects is presented in Table 2, and the contribution is divided into direct and indirect effects as shown in Fig. 9. For the positive angular effect, models (1) - (3) in Table 2 present the regression result of Eqs. (10) – (12), demonstrating the pathways by which the landscape affects the magnitude of the angular effect. First, all landscape factors significantly affected the magnitude of the angular effect at the 0.01 level (see model (1) in Table 2). Second, all landscape factors affected light emission (the mediator, see model (2) in Table 2). Third, the light emission in each grid cell significantly affected the magnitude of the angular effect when controlling for landscape factors (model (3) in Table 2). Fourth, the coefficients (c' in Eq. (12)) and the significance of landscape factors changed after we controlled for light emissions (model (3) in Table 2). The analysis demonstrated that light emissions partially mediated the impact of NDVI, building- and road-related variables.

Table 2. Estimated results of the three regressions of Eqs. (10) - (12) of mediation analysis for positive and negative angular effects, coefficients of city fixed-effect dummy variables not presented.

	Positive			**Negative**		
	(1)	(2)	(3)	(4)	(5)	(6)
	Magnitude	NTL Emission	Magnitude	Magnitude	NTL Emission	Magnitude
Road Length	-0.033***	4.203**	-0.050***	-0.007	5.365	-0.047
NDVI	-0.785***	-132.241***	-0.242***	-1.712***	-284.772***	0.393
Building height	0.150**	95.257***	-0.242***	0.967***	56.457**	0.550**
Building size	0.004***	0.420**	0.002**	-0.033	4.149	-0.063**
Number of Buildings	-0.016***	-2.849***	-0.005***	0.041	3.274	0.017
NTL Emission	-	-	0.004***	-	-	0.007***
Constant	0.556***	98.359***	0.152***	1.119***	187.912***	-0.270
City-fixed effects	Yes	Yes	Yes	Yes	Yes	Yes
Observations	6,826	6,826	6,826	173	173	173
R-squared	0.498	0.508	0.711	0.592	0.839	0.747

t-statistics in parentheses
*** p<0.001, ** p<0.01, * p<0.05

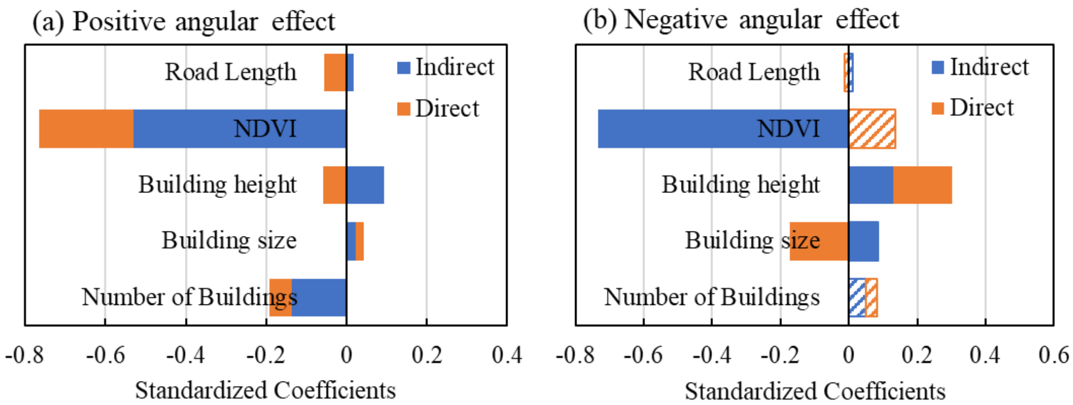

Fig. 9. Impact of the total (stacked bars), indirect (blue sections), and direct effect (orange sections) for each landscape factor in positive angular effect (a) and negative angular effect (b) measured by standardized coefficients. The sections with blue and orange string-pattern-filled bars indicate nonsignificant indirect and direct effects respectively.

NDVI is one of the major contributors diminishing the magnitude of the positive angular effect (Fig. 9 (a)). As artificial light emissions are inversely proportional to NDVI (Zhang et al., 2013), NDVI can indirectly reduce the magnitude of the angular effect by lowering light emissions indirectly. Additionally, vegetation may directly reduce the magnitude by obstructing lights that are supposed to be visible at a large VZA. Building height was another noteworthy influential factor causing opposing direct and indirect effects on the magnitude of the positive angular effect and eventually weakening its magnitude. The positive indirect effect indicated that the building height increased the magnitude of the angular effect by raising light emission from light-emitting façades such as windows and illuminated signs. The negative direct effect indicated that taller buildings inhibited an increase of obliquely observed NTL radiance.

The building size and amount mainly contribute to promoting and diminishing the magnitude of the positive angular effect respectively. As demonstrated in Section 4.1, the positive angular effect was usually present in residential areas (dense houses) or industrial areas (plants and factories with large footprints). Therefore, a larger average building size indicated more artificial light (indirect effect) and more floodlit or illuminated vertical surfaces (direct effect). The effect in the number of buildings also conformed with the relationship between land use and light emission: residential areas tend to have more buildings but are dimmer than industrial areas.

For the negative angular effect, the analysis results suggest that NDVI is the primary restraint on the magnitude of the negative angular effect, while the building height is the primary contributor. The regression results for Eqs. (10) – (12) are listed in Models (4) - (6) in Table 2, and the significance of direct and indirect effects are illustrated in Fig. 9 (b). NDVI strongly reduced the magnitude of the negative angular effect through only the indirect pathway (i.e., full mediation). Since the magnitude of the negative angular effect indicated that the slope of observed NTL brightness decreased with the VZA, the inverse relationship between vegetation and light emission resulted in a weakening angular effect through the mediator. The building height provided the most decisive contribution to the magnitude of the angular effect by directly blocking artificial light. For building size, there a suppression effect was observed: the direct and indirect effects were both significant but of opposite signs, leading to a nonsignificant total effect on the dependent variable.

For the U-shaped angular effect, results of drop and rise segments (Fig. 10) are generally consistent with the negative and positive angular effects respectively, suggesting that the impact of landscape factors on the U-shaped angular effect is kind of a combination of negative and positive angular effects. Specifically, for the indirect effect, road length, NDVI, building height, and the number of buildings have significant ($p<0.01$) impact on the magnitude of angular effects through affecting the light emission, and the impact of each factor is in the same direction for both drop and rise segments. For example, NDVI can indirectly reduce the magnitude of angular effect in both drop (-0.563) and rise (-0.310) segments because of its inverse relationship with artificial light emissions.

For the direct effect, both NDVI and building height have significant ($p<0.001$) opposite impacts between drop and rise segments in the U-shaped angular effect. For example, NDVI positively affects the magnitude of angular effect in the drop segment (0.075) but negatively (-0.253) in the rise segment. Building height has a direct impact on the drop and rise segments (0.082 vs. -0.156) like NDVI. It suggests that in the landscape with U-shape angular effect (green areas in Fig. 8 (b)), both trees and buildings could block more upwards artificial lights when viewing angle changes from nadir to a middle turning point (e.g., VZA=30 degree), which amplifies the drop of NTL with VZA (i.e., causing large magnitude in the drop segment). On the contrary, more artificial lights are observed when the viewing angle changes from the middle turning point to a large angle (e.g., VZA=60 degree), which forms the rise segment, but the block effect from both trees and buildings weakens this increase that leads to a negative contribution of NDVI and building height to the magnitude of angular effect in the rise segment.

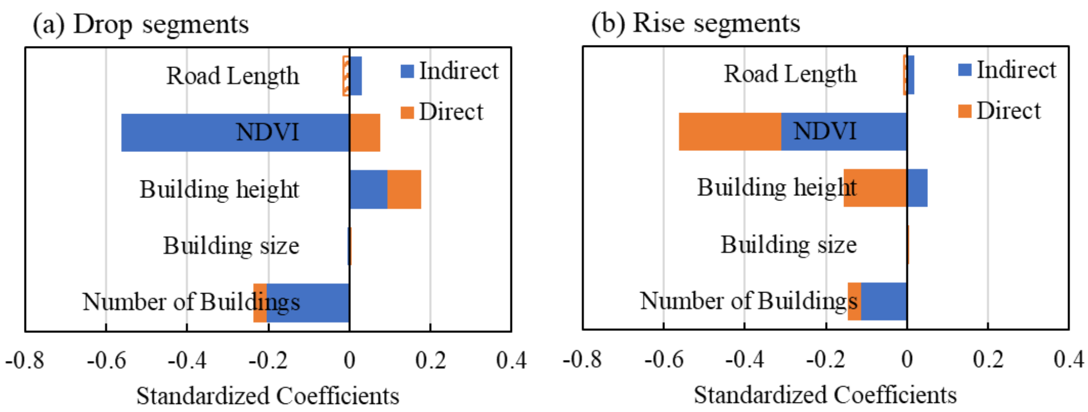

Fig. 10. Impact of the total (stacked bars), indirect (blue sections), and direct effect (orange sections) for each landscape factor in drop segments of U-shaped angular effect (a) and rise segments of U-shaped angular effect (b) measured by standardized coefficients. The sections with blue and orange string-pattern-filled bars indicate nonsignificant indirect and direct effects respectively.

5 Discussion

5.1 Rationale of the conceptual model

In this research, we built a conceptual model to analyze the sources of the angular effect in cities from two aspects: the variance in light visibility and blocking along with changes in the satellite viewing angle. On this basis, several landscape indicators related to light visibility and blocking were selected to model the direction and magnitude of the angular effect. To further verify the rationality of the conceptual model, we simulated changes in light visibility and blocking with viewing angles using the 3D city model. Three neighboring samples (1.5-km blocks at 34°02′N, 118°15′) with different angular effect directions were selected in Los Angeles. The Google Earth 3D image in Fig. 11 (a) shows the distinctive landscape of the three samples. The sample for the negative angular effect was located in the CBD of Los Angeles, which is densely populated with high-rise buildings. The sample for the U-shaped angular effect was located in an industrial area with buildings of large footprints and moderate heights, while the positive angular effect sample was located in a residential area with dense low-rise houses.

Since streetlights are the primary source of nighttime artificial light (Bará et al., 2019), we estimated the visibility of streets based on the 3D city model at different viewing angles (Fig. 11 (b)). Blocks with negative and U-shaped angular effects possess more road area, and the visible area of roads declined with the VZA in all three types of samples, with the most dramatic drops in the negative angular effect block, while the road visibility in the positive angular effect block declined only slightly.

Another light source, building surfaces, was also simulated using the 3D city model. Fig. 11 (c) shows the variation in the blocking ratio, i.e., the proportion of the building surface that is blocked by surrounding buildings. The building surface visibility with and without considering the blocking effect was plotted as the dashed and solid lines in Fig. 11 (d), respectively. The visible building surface was calculated as the sum of the projected areas of the building surface in the vertical direction of the satellite's line of sight. The surface area of the building (potential light sources) was more significant in the negative angular effect area due to the tall densely positioned buildings, where the obscured portion increases dramatically with viewing angle. The visibility of building surface changes in positive and U-shaped areas were similar; both first increased and then slightly decreased at large viewing angles. Note that the simulation of visibility and blocking effects of building surfaces can only partially explain the angular effect. Because the surface luminance of buildings varies with the building functions and materials, the surface luminance may constitute only a tiny fraction of the observed radiance (Bará et al., 2019). In general, the characteristics of angular effects conform to the simulation results for the corresponding visibility and blocking, demonstrating the rationale of the proposed conceptual model.

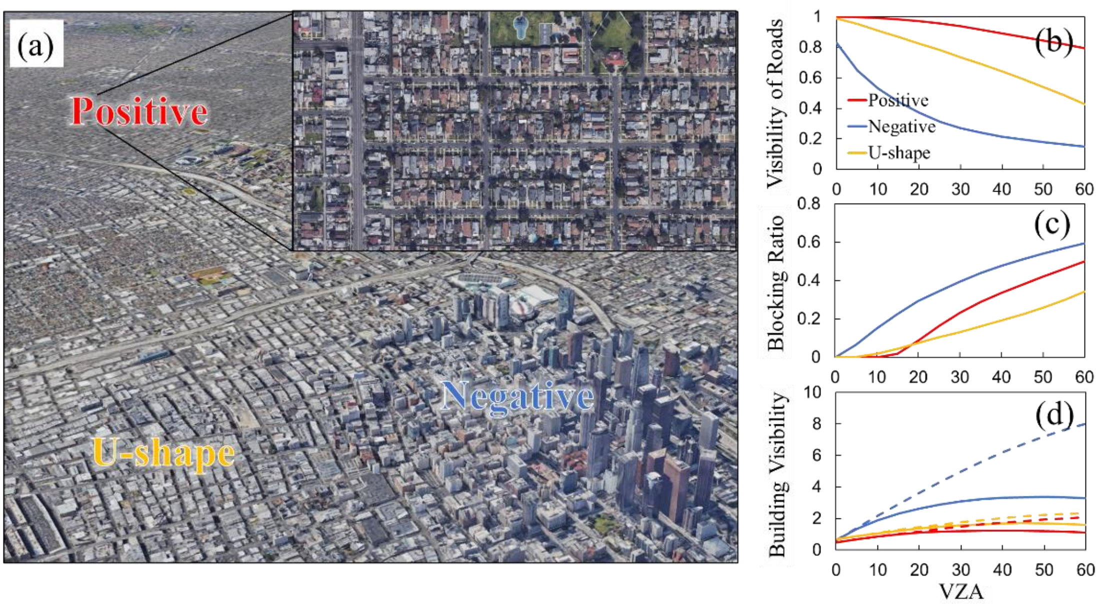

Fig. 11. Simulated light variation with viewing angle for three samples of different angular effects: (a) Location and Google Earth 3D images of the three samples; (b) Estimated visibility of roads; (c) Estimated blocking ratio of building surface; (d) Estimated building visibility. Solid curves are sums of the projected building surface areas in the vertical direction of the satellite's line-of-sight, and the dashed curves are the visible building surface considering the blocking effect of surrounding buildings.

Furthermore, to examine the reliability of the proposed model, we validated the mediation analysis model built from NTL data in 2014 by predicting the magnitude of the angular effect of NTL data in 2016. The predicted magnitude was compared with the observed magnitude that was directedly derived from the NTL data of our study area in 2016 (Fig. 12). The validation data is two years later than the data for building the model, which can ensure the independence between training data and validation data. As shown in Fig. 12, there is a high consistency between predicted angular changes and satellite observed angular changes in 2016 (r-squared: 0.76), suggesting that the proposed model is reasonable and is applicable to predict the angular effect of NTL images in different years.

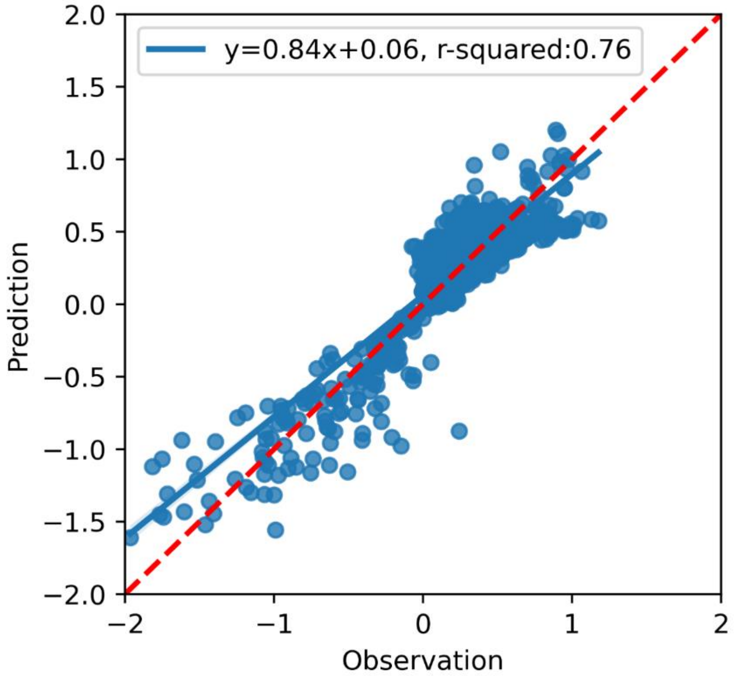

Fig. 12. Scatter plot for the observed and predicted magnitude of the angular effect in 2016.

5.2 Impact of angular effects on city-scale studies

NTL time series is widely used to conduct analyses at the urban scale (Elvidge et al., 2020; Román & Stokes, 2015). To clarify the possibility of bias induced by angular effects, we examined the relationship between the average NTL and VZA at the city scale. As observations contaminated by clouds, snow, and other anomalies were filtered out as stated in Section 3.2, we selected only days where a valid grid cell exceeded 60% of the urban area. Fig. 13 demonstrates that a significant angular effect exists for the standardized mean NTL radiance, with the radiance at a zenith angle of 60° being approximately 1.6 - 4 times higher than those observed at zenith. As specified in Section 4.1, the spatial pattern of angular effects was positive in most areas of the selected cities; thus, all cities except Boston presented positive trends, as shown in Fig. 13

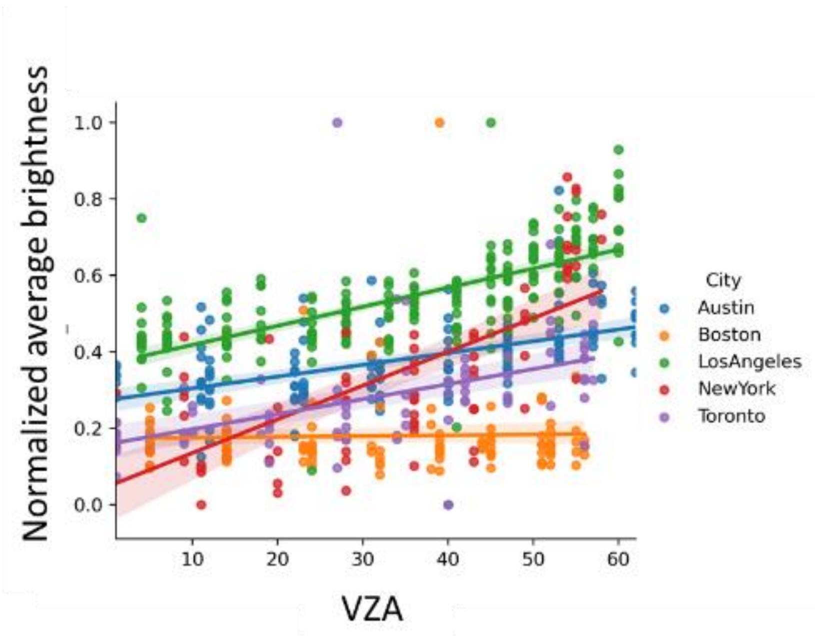

Fig. 13. The scatter plot and trends of the VZA and normalized NTL radiance at city scale.

This city-scale angular effect is a convergence of different angular effects at pixel scale within the designated area; therefore, the angular effect at city scale depends on the overall landscape of the city. To verify the relationship in other cities, we calculated the city-scale angular effect for Hong Kong and Beijing compared with Los Angeles (Fig. 14 (a)). As shown in the building height map (Fig. 14 (b)), 3D city model and Google Earth 3D images (Fig. 14 (c)), cities like Los Angeles have landscape patterns with dense concentrations of high-rise buildings in their CBDs, and low-rise-dominated residential and industrial areas occupy most of the remainder of the cities, forming an overall positive angular effect. Hong Kong, on the other hand, is a typical city with high-density tall buildings and has an overall landscape similar to the CBD in cities like Los Angeles, leading to a negative urban-scale angular effect. In contrast, Beijing has a much more mixed landscape with buildings of very different heights in the same neighborhood, leading to an unapparent overall angular effect.

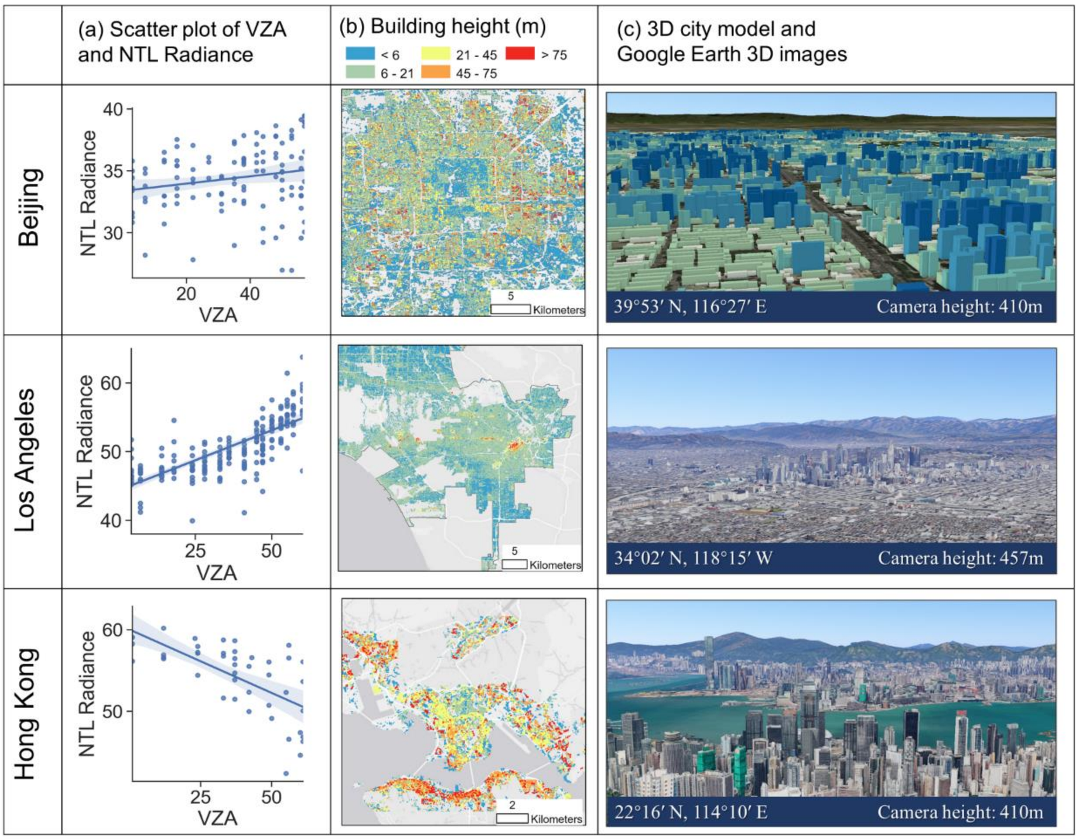

Fig. 14. City-scale angular effect and corresponding urban landscape. (a) Scatter plot of VZA and NTL radiance in the three cities; (b) Building height maps with unified color bar; (c) 3D city model (Beijing) and Google Earth 3D images (Los Angeles and Hong Kong).

5.3 Implications and limitations

In this research, we propose a conceptual model to characterize the sources of the angular effect in satellite NTL observations. By leveraging the statistical models and city 3D model, we modeled the direction and magnitude of the angular effect and investigated the impacts of various urban landscapes on them. Wide-view sensors have been recognized to lead to high variations in NTL radiance observations (Coesfeld et al., 2018). Angular observations are therefore not usually preferred, as they often lead to inconsistency among multiple observations, which makes mosaicking or comparing them over time a great challenge. However, at the same time, angular observations provide valuable structural and vertical information about urban areas but have not been fully interpreted or utilized (Levin et al., 2020).

This study offers several implications for future research on NTL regarding the abovementioned research gaps. First, this research reveals the impacts of landscape indicators on the direction and magnitude of the angular effect, providing vital information for further understanding the angular effect by developing physical models such as ray-tracing models. Second, the findings provide insights into interpretations of structural and vertical information using angular NTL observations from VIIRS/DNB or DMSP/OLS. Finally, this research provides useful information for building an angular effect correction model to reconstruct daily NTL time series and benefits to monitor high-frequency socioeconomic dynamics.

However, there are several limitations that need to be improved in future research. First, considering the diverse directions of ground light sources, we assumed that the anisotropic reflections canceled each other out, and this study mainly concentrated on the variance in light visibility and blocking when building the conceptual and statistical models. Second, the angular effects are considered only based on VZA since satellite viewing azimuth angles mostly concentrated in two angles that forming similar zenith angular effect, but the azimuth angle may significantly affect the NTL observations if the light sources are not symmetrically distributed in the east and west sides. Third, this study assumed that all selected cities have year-round stable artificial lights, but some pixels may experience short-term changes that introduce errors in the calculation of the direction and magnitude of the angular effect. Future studies can design UAV experiments to measure the artificial light intensity over the same area from different angles during a short period to avoid the disturbance of light changes.

6 Conclusion

Angular effects have been proven to exist in satellite-observed NTL images and vary from place to place. However, whether there is a spatial pattern and how urban morphology contributes to the angular effect remain unknown. To answer these questions, we investigated the angular effect and its drivers in both direction and magnitude. First, we proposed a conceptual model of the angular effect and hypothesized the mechanism by which the angular effect was formed. Second, by characterizing the angular effect and investigating their spatial distribution in five representative cities, we found three types of angular effects with distinct directions, i.e., negative, U-shaped, and positive. A dramatic shift in the direction of the angular effect was found from the city center outwards: a negative angular effect was present in the city center, while U-shaped and positive angular effects were primarily present outside the CBD, which was consistent with the hypothesized pattern of the angular effect from the conceptual model. Finally, we quantified the impacts of landscape factors on the direction and magnitude of the angular effect using multinomial logistic regression and mediation analysis, respectively.

The results suggested that the direction of the angular effect was mainly controlled by urban morphology, especially the building height, which determined the visible and blocked portions of artificial light. The magnitude of the angular effect was determined by landscape through two pathways: direct effect (by affecting the blocked and visible portion of the light) and indirect effect (by affecting artificial light emission). The model estimation showed that the magnitude of the angular effect was due to the direct and indirect effects of NDVI and building characteristics. Specifically, NDVI and building height were the main factors that reduced and increased the magnitude of the positive angular effect, respectively. The building height had opposing direct and indirect effects, which ultimately weakened the magnitude of the positive angular effect. For the negative angular effect, the indirect effect of NDVI was the primary constraint, while the direct effect of building height was the most decisive contributor. The major contributors of the drop and rise segments of the U-shaped angular effect are generally consistent with the negative and positive angular effect, respectively, suggesting that the impact of landscape factors on the U-shaped angular effect is a combination of the negative and positive ones. In addition, we quantified the angular effect at the city scale and found that the overall angular effect was also significant and determined by the landscape at urban scale. These findings enrich our understanding of the angular effect, enlighten the development of an angular effect correction model to reconstruct a high-quality daily NTL time series, and contribute to better monitoring high-frequency socioeconomic dynamics.

Acknowledgments

This study was supported by the National Natural Science Foundation of China (Project No.42022060), and the Hong Kong Polytechnic University (Project No. ZVN6). We thank Dr. Xi Li and Miss Yi Nam Xu for their constructive comments and suggestions to improve this manuscript.

Appendix A. Supplementary data

Supplementary data to this article can be found online at ###

References

Bai, Y., Cao, C., & Shao, X. (2015). Assessment of scan-angle dependent radiometric bias of Suomi-NPP VIIRS day/night band from night light point source observations. *Earth Observing Systems XX*, *9607*, 960727. https://doi.org/10.1117/12.2187119

Bará, S., Rodríguez-Arós, Pérez, M., Tosar, B., Lima, R. C., Sánchez de Miguel, A., & Zamorano, J. (2019). Estimating the relative contribution of streetlights, vehicles, and residential lighting to the urban night sky brightness. *Lighting Research and Technology*, *51*(7), 1092–1107. https://doi.org/10.1177/1477153518808337

Baron, R. M., & Kenny, D. A. (1986). The Moderator-Mediator Variable Distinction in Social Psychological Research. Conceptual, Strategic, and Statistical Considerations. *Journal of Personality and Social Psychology*, *51*(6), 1173–1182. https://doi.org/10.1037/0022-3514.51.6.1173

Cao, C., Bai, Y., Wang, W., & Choi, T. (2019). Radiometric inter-consistency of

VIIRS DNB on Suomi NPP and NOAA-20 from observations of reflected lunar lights over deep convective clouds. *Remote Sensing*, *11*(8). https://doi.org/10.3390/rs11080949

Cao, C., Shao, X., & Uprety, S. (2013). Detecting light outages after severe storms using the S-NPP/VIIRS day/night band radiances. *IEEE Geoscience and Remote Sensing Letters*, *10*(6), 1582–1586. https://doi.org/10.1109/LGRS.2013.2262258

Coesfeld, J., Anderson, S. J., Baugh, K., Elvidge, C. D., Schernthanner, H., & Kyba, C. C. M. (2018). Variation of individual location radiance in VIIRS DNB monthly composite images. *Remote Sensing*, *10*(12), 1–17. https://doi.org/10.3390/rs10121964

Elliott, R. J. R., Strobl, E., & Sun, P. (2015). The local impact of typhoons on economic activity in China: A view from outer space. *Journal of Urban Economics*, *88*, 50–66. https://doi.org/10.1016/j.jue.2015.05.001

Elvidge, C. D., Ghosh, T., Hsu, F. C., Zhizhin, M., & Bazilian, M. (2020). The dimming of lights in China during the COVID-19 pandemic. *Remote Sensing*, *12*(17). https://doi.org/10.3390/RS12172851

Elvidge, C. D., Sutton, P. C., Ghosh, T., Tuttle, B. T., Baugh, K. E., Bhaduri, B., & Bright, E. (2009). A global poverty map derived from satellite data. *Computers and Geosciences*, *35*(8), 1652–1660. https://doi.org/10.1016/j.cageo.2009.01.009

Elvidge, C. D., Zhizhin, M., Baugh, K., Hsu, F. C., & Ghosh, T. (2016). Methods for global survey of natural gas flaring from visible infrared imaging radiometer suite data. *Energies*, *9*(1). https://doi.org/10.3390/en9010014

Fu, D., Xia, X., Duan, M., Zhang, X., Li, X., Wang, J., & Liu, J. (2018). Mapping nighttime PM2.5 from VIIRS DNB using a linear mixed-effect model. *Atmospheric Environment*, *178*(January), 214–222. https://doi.org/10.1016/j.atmosenv.2018.02.001

Ge, W., Yang, H., Zhu, X., Ma, M., & Yang, Y. (2018). Ghost city extraction and rate estimation in China based on NPP-VIIRS night-time light data. *ISPRS International Journal of Geo-Information*, *7*(6). https://doi.org/10.3390/ijgi7060219

Hayes, A. F. (2017). *Introduction to mediation, moderation, and conditional process analysis: A regression-based approach*. Guilford publications.

Imhoff, M. L., Lawrence, W. T., Stutzer, D. C., & Elvidge, C. D. (1997). A technique for using composite DMSP/OLS "city lights" satellite data to map urban area. *Remote Sensing of Environment*, *61*(3), 361–370. https://doi.org/10.1016/S0034-4257(97)00046-1

Johnson, R. S., Zhang, J., Hyer, E. J., Miller, S. D., & Reid, J. S. (2013). Preliminary investigations toward nighttime aerosol optical depth retrievals from the VIIRS

Day/Night Band. *Atmospheric Measurement Techniques*, *6*(5), 1245–1255. https://doi.org/10.5194/amt-6-1245-2013

Kyba, C. C. M., Garz, S., Kuechly, H., de Miguel, A. S., Zamorano, J., Fischer, J., & Hölker, F. (2015). High-resolution imagery of earth at night: New sources, opportunities and challenges. *Remote Sensing*, *7*(1), 1–23. https://doi.org/10.3390/rs70100001

Kyba, C. C. M., Kuester, T., De Miguel, A. S., Baugh, K., Jechow, A., Hölker, F., Bennie, J., Elvidge, C. D., Gaston, K. J., & Guanter, L. (2017). Artificially lit surface of Earth at night increasing in radiance and extent. *Science Advances*, *3*(11), 1–9. https://doi.org/10.1126/sciadv.1701528

Kyba, C. C. M., Ruhtz, T., Lindemann, C., Fischer, J., & Hölker, F. (2013). Two camera system for measurement of urban uplight angular distribution. *AIP Conference Proceedings*, *1531*(May), 568–571. https://doi.org/10.1063/1.4804833

Levin, N. (2017). The impact of seasonal changes on observed nighttime brightness from 2014 to 2015 monthly VIIRS DNB composites. *Remote Sensing of Environment*, *193*, 150–164. https://doi.org/10.1016/j.rse.2017.03.003

Levin, N., Kyba, C. C. M., Zhang, Q., Sánchez de Miguel, A., Román, M. O., Li, X., Portnov, B. A., Molthan, A. L., Jechow, A., Miller, S. D., Wang, Z., Shrestha, R.

M., & Elvidge, C. D. (2020). Remote sensing of night lights: A review and an outlook for the future. *Remote Sensing of Environment, 237*(October 2018), 111443. https://doi.org/10.1016/j.rse.2019.111443

Li, X., Li, D., Xu, H., & Wu, C. (2017). Intercalibration between DMSP/OLS and VIIRS night-time light images to evaluate city light dynamics of Syria's major human settlement during Syrian Civil War. *International Journal of Remote Sensing*, *38*(21), 5934–5951. https://doi.org/10.1080/01431161.2017.1331476

Li, X., Ma, R., Zhang, Q., Li, D., Liu, S., He, T., & Zhao, L. (2019). Anisotropic characteristic of artificial light at night – Systematic investigation with VIIRS DNB multi-temporal observations. *Remote Sensing of Environment*, *233*(August). https://doi.org/10.1016/j.rse.2019.111357

MacKinnon, D. P., Warsi, G., & Dwyer, J. H. (1995). A Simulation Study of Mediated Effect Measures. *Multivariate Behavioral Research*, *30*(1), 41–62. https://doi.org/10.1207/s15327906mbr3001_3

Polivka, T. N., Wang, J., Ellison, L. T., Hyer, E. J., & Ichoku, C. M. (2016). Improving Nocturnal Fire Detection with the VIIRS Day-Night Band. *IEEE Transactions on Geoscience and Remote Sensing*, *54*(9), 5503–5519. https://doi.org/10.1109/TGRS.2016.2566665

Preacher, K. J., & Hayes, A. F. (2008). Asymptotic and resampling strategies for assessing and comparing indirect effects in multiple mediator models. *Behavior Research Methods*, *40*(3), 879–891. https://doi.org/10.3758/BRM.40.3.879

Román, M. O., & Stokes, E. C. (2015). Holidays in lights: Tracking cultural patterns in demand for energy services. *Earth's Future*, *3*(6), 182–205. https://doi.org/10.1002/2014EF000285

Román, M. O., Wang, Z., Sun, Q., Kalb, V., Miller, S. D., Molthan, A., Schultz, L., Bell, J., Stokes, E. C., Pandey, B., Seto, K. C., Hall, D., Oda, T., Wolfe, R. E., Lin, G., Golpayegani, N., Devadiga, S., Davidson, C., Sarkar, S., … Masuoka, E. J. (2018). NASA's Black Marble nighttime lights product suite. *Remote Sensing of Environment*, *210*, 113–143. https://doi.org/10.1016/j.rse.2018.03.017

Shi, K., Chen, Y., Li, L., & Huang, C. (2018). Spatiotemporal variations of urban CO2 emissions in China: A multiscale perspective. *Applied Energy*, *211*, 218–229. https://doi.org/10.1016/j.apenergy.2017.11.042

Tong, K. P., Kyba, C. C. M., Heygster, G., Kuechly, H. U., Notholt, J., & Kolláth, Z. (2020). Angular distribution of upwelling artificial light in Europe as observed by Suomi–NPP satellite. *Journal of Quantitative Spectroscopy and Radiative Transfer*, *249*, 107009. https://doi.org/10.1016/j.jqsrt.2020.107009

Wang, J., Aegerter, C., Xu, X., & Szykman, J. J. (2016). Potential application of VIIRS Day/Night Band for monitoring nighttime surface PM2.5 air quality from space. *Atmospheric Environment*, *124*, 55–63. https://doi.org/10.1016/j.atmosenv.2015.11.013

Wang, J., Roudini, S., Hyer, E. J., Xu, X., Zhou, M., Garcia, L. C., Reid, J. S., Peterson, D. A., & da Silva, A. M. (2020). Detecting nighttime fire combustion phase by hybrid application of visible and infrared radiation from Suomi NPP VIIRS. *Remote Sensing of Environment*, *237*, 111466. https://doi.org/10.1016/j.rse.2019.111466

Wang, J., Zhou, M., Xu, X., Roudini, S., Sander, S. P., Pongetti, T. J., Miller, S. D., Reid, J. S., Hyer, E., & Spurr, R. (2020). Development of a nighttime shortwave radiative transfer model for remote sensing of nocturnal aerosols and fires from VIIRS. *Remote Sensing of Environment*, *241*, 111727. https://doi.org/10.1016/j.rse.2020.111727

Wang, Z., Román, M. O., Kalb, V. L., Miller, S. D., Zhang, J., & Shrestha, R. M. (2021). Quantifying uncertainties in nighttime light retrievals from Suomi-NPP and NOAA-20 VIIRS Day/Night Band data. *Remote Sensing of Environment*, *263*. https://doi.org/10.1016/j.rse.2021.112557

Zeng, X., Shao, X., Qiu, S., Ma, L., Gao, C., & Li, C. (2018). Stability monitoring of the VIIRS day/night band over dome C with a lunar irradiance model and BRDF correction. *Remote Sensing*, *10*(2). https://doi.org/10.3390/rs10020189

Zhang, Q., Schaaf, C., & Seto, K. C. (2013). The Vegetation adjusted NTL Urban Index: A new approach to reduce saturation and increase variation in nighttime luminosity. *Remote Sensing of Environment*, *129*, 32–41. https://doi.org/10.1016/j.rse.2012.10.022

Zhao, M., Zhou, Y., Li, X., Cao, W., He, C., Yu, B., Li, X., Elvidge, C. D., Cheng, W., & Zhou, C. (2019). Applications of satellite remote sensing of nighttime light observations: Advances, challenges, and perspectives. *Remote Sensing 11*(17), 1971. https://doi.org/10.3390/rs11171971

Zhao, Xinshu, Lynch, J. G., & Chen, Q. (2010). Reconsidering Baron and Kenny: Myths and truths about mediation analysis. *Journal of Consumer Research*, *37*(2), 197–206. https://doi.org/10.1086/651257

Zhao, Xizhi, Yu, B., Liu, Y., Yao, S., Lian, T., Chen, L., Yang, C., Chen, Z., & Wu, J. (2018). NPP-VIIRS DNB daily data in natural disaster assessment: Evidence from selected case studies. *Remote Sensing*, *10*(10), 1–25. https://doi.org/10.3390/rs10101526

Zhou, M., Wang, J., Chen, X., Xu, X., Colarco, P. R., Miller, S. D., Reid, J. S., Kondragunta, S., Giles, D. M., & Holben, B. (2021). Nighttime smoke aerosol optical depth over U.S. rural areas: First retrieval from VIIRS moonlight observations. *Remote Sensing of Environment*, *267*, 112717.

https://doi.org/10.1016/j.rse.2021.112717

Zhou, Y., Li, X., Asrar, G. R., Smith, S. J., & Imhoff, M. (2018). A global record of annual urban dynamics (1992–2013) from nighttime lights. *Remote Sensing of Environment*, *219*, 206–220. https://doi.org/10.1016/j.rse.2018.10.015

List of Figure Captions

Fig. 1. Location and Google Earth 3D images of the five selected cities. Background NTL image from NASA (https://earthobservatory.nasa.gov/features/NightLights).

Fig. 2. Sketch of the conceptual model depicting three typical sources of the angular effect: (1) blocking effect, (2) visibility changes, and (3) surface reflectance and BRDF.

Fig. 3. Samples of angular effect and landscape. (a) Google Earth 3D image around the Los Angeles CBD; (b) VZA-NTL scatters of the negative angular effect samples at site A; (c) VZA-NTL scatters of the positive angular effect samples at site B; (d) VZA-NTL scatter diagrams of the U-shape angular effect samples at site C.

Fig. 4. Examples of extracting stable VZA-NTL pairs using the orbit-based

composition method. The blue dots are NTL radiance observations, orange dots are the stable VZA-NTL pairs extracted, and orange curves show the direction of the angular effect. Location of site A, B, and C show in Fig. 3 (a).

Fig. 5. Classification workflow to identify the direction of the angular effect for each grid cell.

Fig. 6. Sketch of mediation analysis: (a) The overall relationship between independent and dependent variables; (b) The direct and indirect effects between independent and dependent variables.

Fig. 7. Scatter plots of VZA and NTL radiance for typical samples. The blue dots are NTL observations, and orange curves show the direction of the angular effect detected from stable VZA-NTL pairs (orange dots).

Fig. 8. (a) Spatial distribution of annual average NTL brightness, the pink dashed circle shows the buffer zones at an interval of 5 km and the brightest region as the center; (b) Spatial distribution of different angular effect directions; (c) Building height maps; (d) Changes in average NTL radiance (orange curve) and angular effect

coefficient (purple curve) outwards from the urban center. The shadow represents the standard deviation.

Fig. 9. Impact of the total (stacked bars), indirect (blue sections), and direct effect (orange sections) for each landscape factor in positive angular effect (a) and negative angular effect (b) measured by standardized coefficients. The sections with blue and orange string-pattern-filled bars indicate nonsignificant indirect and direct effects respectively.

Fig. 10. Impact of the total (stacked bars), indirect (blue sections), and direct effect (orange sections) for each landscape factor in drop segments of U-shaped angular effect (a) and rise segments of U-shaped angular effect (b) measured by standardized coefficients. The sections with blue and orange string-pattern-filled bars indicate nonsignificant indirect and direct effects respectively.

Fig. 11. Simulated light variation with viewing angle for three samples of different angular effects: (a) Location and Google Earth 3D images of the three samples; (b) Estimated visibility of roads; (c) Estimated blocking ratio of building surface; (d) Estimated building visibility. Solid curves are sums of the projected building surface

areas in the vertical direction of the satellite's line-of-sight, and the dashed curves are the visible building surface considering the blocking effect of surrounding buildings.

Fig. 12. Scatter plot for the observed and predicted magnitude of the angular effect in 2016.

Fig. 13. The scatter plot and trends of the VZA and normalized NTL radiance at city scale.

Fig. 14. City-scale angular effect and corresponding urban landscape. (a) Scatter plot of VZA and NTL radiance in the three cities; (b) Building height maps with unified color bar; (c) 3D city model (Beijing) and Google Earth 3D images (Los Angeles and Hong Kong).